Inorganic Chemistry

pubs.acs.org/IC

Article

Formal Cu(III) Species Featuring Dangling Hypochlorite

Raju Eerlapally, Purva Dua, Divya Lakshmi Hareendran, Asterios Charisiadis, Lucia Velasco, Maxime Sauvan, Indresh Verma, Dooshaye Moonshiram,* Gopalan Rajaraman,* and Apparao Draksharapu*

Cite This: *Inorg. Chem.* 2025, 64, 13103−13114

Read Online

ACCESS | Metrics & More | Article Recommendations | Supporting Information

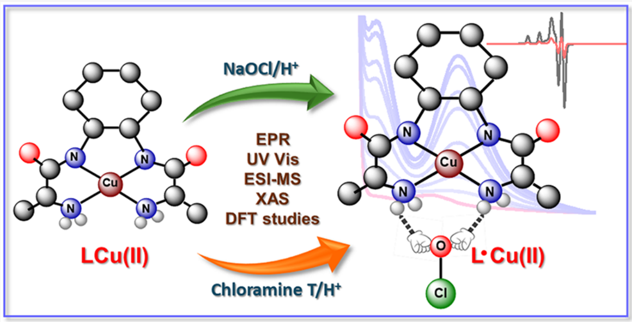

ABSTRACT: In nature, halogenation of organic compounds is performed by two different types of enzymes: halogenases and haloperoxidases. One type halogenates the substrate's C−H bond through metal-hypochlorite intermediates (*i.e.*, Fe^{III}−OCl and V^{V}−OCl), while the other utilizes HOCl hydrogen-bonded within the enzyme channels. Inspired by the vital role of these enzymes, we attempted to characterize a *formal* Cu(III) complex with dangling hypochlorite (**2**), supported by a C_2 symmetric pseudopeptide ligand. **2** was characterized using UV/vis absorption, EPR, XAS, and resonance Raman spectroscopies. Resonance Raman spectroscopic data indicate that the OCl^- ion does not coordinate to the copper center. Furthermore, we employed computational analysis to test our experimental hypothesis, which suggests that $(L^{\bullet+})$Cu(II)/*formal* Cu(III) with dangling hypochlorite hydrogen bonded to the -NH_2 groups of the ligand is the energetically favored ground state structure. The species reported here is unique, as it represents the distinctive example where hypochlorite is bound to the secondary coordination sphere rather than directly coordinating with the metal center. **2** can perform hydrogen atom abstraction reactions on 4-X-2,6-di*tert*-butyl phenol (X = H, Me, OMe, ^{t}Bu) derivatives.

■ INTRODUCTION

Naturally occurring halogenated compounds, especially those found in terrestrial and marine organisms like algae, fungi, sponges, corals, and seaweeds, are potential sources of compounds with antimicrobial activity.[1,2] The secondary metabolites in these organisms serve as a defensive mechanism that can be chemically synthesized and utilized for pharmacological applications.[2,3] Many contain chlorine, which is primarily responsible for their suitability in pharmaceutical chemistry. Exploring the biological activity of these halogenated compounds has led to the discovery of their anticancer, antimicrobial, and antiviral properties.[1] In nature, two distinct metalloenzymatic systems can halogenate organic compounds: nonheme and heme-dependent enzymes, which use O_2 and H_2O_2, respectively. SyrB2 is a nonheme Fe(II) dependent halogenase used in the biosynthesis of the antifungal agent syringomycin. In the proposed catalytic cycle of SyrB2, (Cl)Fe(IV)═O serves as an active intermediate for abstracting a hydrogen atom from the substrate, resulting in the formation of (Cl)Fe(III)−OH and a substrate radical. Subsequent substrate chlorination occurs through a rebound mechanism.[4−6] A similar kind of enzyme found in nature is CytC3, which undergoes halogenation of organic substrates using (Cl)Fe(IV)═O as an active intermediate.[7] However, in the case of heme-dependent enzymes such as iron- and vanadium-containing haloperoxidases, substrate halogenation follows a different mechanistic pathway. For example, in iron-dependent haloperoxidases, the pathway involves the initial formation of $(Porph^{\bullet+})$Fe(IV)═O (Compound-I), which further reacts with a halide ion to form the active intermediate, Fe(III)-OX (where X = Cl and Br) (Figure 1).

Another class of enzymes that do not contain metal is flavin-dependent halogenases, which facilitate substrate halogenation.[8] Examples of flavin-dependent halogenases include PrnA (tryptophan 7-halogenase) and PrnC (monodechloroaminopyrrolnitrin 3-halogenase). In their catalytic pathway, activated flavin adenine dinucleotide (FAD) reacts with dioxygen to produce FAD-OOH, which subsequently converts to FAD−OH and HOCl. The K79 residue forms a hydrogen bond with HOCl, ensuring it remains within the enzyme's channel. The electrophilic attack of hypochlorous acid on the C7 position of tryptophan generates an intermediate carbocation, whose

Received: March 20, 2025
Revised: June 13, 2025
Accepted: June 18, 2025
Published: June 26, 2025

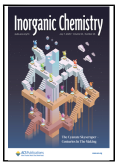

https://doi.org/10.1021/acs.inorgchem.5c01273
Inorg. Chem. 2025, 64, 13103−13114

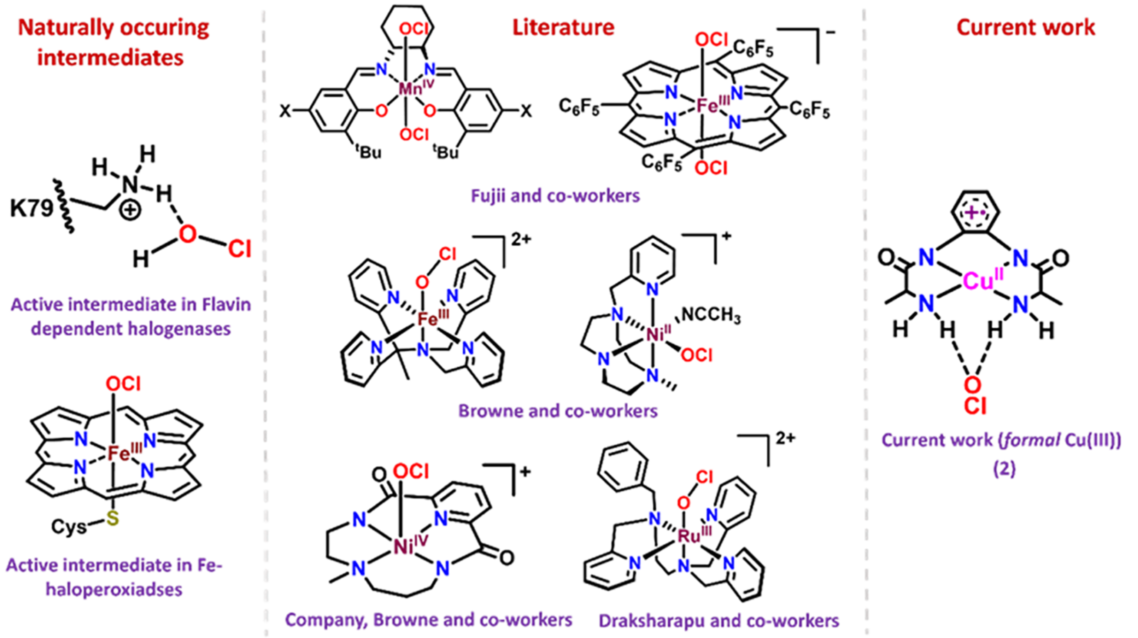

Figure 1. Spectroscopically characterized high-valent metal hypochlorite species to date. *Note: In the case of Flavin-dependent halogenases, the substrate is not shown for clarity.*

deprotonation via the E346 residue leads to the chlorination of tryptophan (Figure 1).[9]

Inspired by nature's selection, researchers tried to replicate biological systems to deepen the understanding of these processes. In this context, Fuji and co-workers in 2012 successfully synthesized and spectroscopically characterized $[(TPFP)Fe^{III}(OCl)_2]$ (TPFP = 5,10,15,20-tetrakis(pentafluorophenyl)porphyrinate) at −60 °C. They demonstrated the reactivity of Fe(III)-OCl toward sulfoxidation, chlorination, and epoxidation reactions.[10] Later, the same group, spectroscopically characterized $[(salen)Mn^{IV}(OCl)_2]$ (salen = 6,6′-((1E,1′E)-(((1*R*,2*R*)-cyclohexane-1,2-diyl)bis(azanylylidene))bis(methanylylidene))bis(2,4-di*tert*-butylphenol)) transient species at −20 °C, capable of performing hydrogen atom transfer (HAT) and oxygen atom transfer (OAT) reactions of organic substrates (Figure 1).[11] Browne and co-workers in 2015, described, for the first time, the generation of nonheme $[(MeN4Py)Fe^{III}(OCl)]^{2+}$ (MeN4Py = 1,1-di(pyridin-2-yl)-N,N-bis(pyridin-2-ylmethyl)ethanamine) in water from the reaction of (MeN4Py)Fe(II) with aqueous NaOCl at pH 2.[12] They also established $[(PyTACN)Ni^{II}-OCl]^+$ species using NaOCl as an oxidant and halide transfer reagent.[13] Company, Browne and co-workers shed light on the reactivity of high-valent Ni(IV)-OCl supported by an amide-based macrocyclic ligand. This high-valent Ni(IV)-OCl species is capable of activating strong C−H bonds and performing catalytic oxidation and halogenation.[14] Very recently, our group reported the spectroscopic characterization of $[(BnTPEN)Ru(III)-OCl]^{2+}$ (BnTPEN = N^1-benzyl-N^1,N^2,N^2-tris(pyridine-2-ylmethyl)ethane-1,2-diamine) at ambient temperature, which can perform OAT and hydrogen atom abstraction (HAA) reactions in potential organic substrates (Figure 1).[15,16] Tang and co-workers recently characterized a copper-dependent halogenase, ApnU, which catalyzes the chlorination of unactivated $C(sp^3)$-H bonds. This discovery represents a significant advancement in enzymatic C−H bond functionalization.[17] An extensive literature review suggests that the reported studies discuss the direct binding of hypochlorite to the metal center. However, the hydrogen bonding interaction of ClO^- with high-valent metal intermediates in the secondary coordination sphere has not been accomplished thus far. Herein, we report the synthesis and spectroscopic characterization of an intermediate **2**, in which ClO^- is in proximity to a *formal* Cu(III) complex supported by OPD-alanine pseudopeptide ligand $\mathbf{H_2L}$ ($\mathbf{H_2L}$ = N,N′-(1,2-phenylene)bis(2-aminopropanamide)) through hydrogen bonding. The generated intermediate **2** was characterized using UV/vis absorption, XAS, resonance Raman spectroscopy, and computational studies. Furthermore, intermediate **2** can perform the HAA reaction with trisubstituted phenols. To the best of our knowledge, this is the first example where ClO^- is stabilized by hydrogen bonding interaction with any high-valent metal intermediate, mimicking the flavin-dependent halogenases class of enzymes.

■ RESULTS AND DISCUSSION

The reaction of equimolar concentrations of $Cu^{II}(OAc)_2 \cdot H_2O$ and $\mathbf{H_2L}$ in the presence of KOH in methanol resulted in a purple-colored solution (Scheme S1 and Figures S1−S4). To confirm complete deprotonation of the amide functionalities upon coordination, FT-IR spectra were recorded for the free ligand ($\mathbf{H_2L}$) and **1**. A redshift of the C═O stretching vibration from 1657 cm^{-1} in $\mathbf{H_2L}$ to 1552 cm^{-1} in **1** was observed, consistent with full deprotonation of the amide groups upon coordination to the Cu(II) center (Figure S5).[18] Slow vapor diffusion of ether into this solution produced purple crystals of **1**. The crystallographic analysis of **1** revealed that the asymmetric unit contains four molecules. The X-ray crystal structure of **1**, depicted in Figure 2A, shows that all four nitrogen atoms from the ligand occupied the equatorial positions with a τ value around 0.15, resulting in a distorted square planar geometry around the copper center. The average $Cu-N_{amide}$ and $Cu-N_{amine}$ bond distances are observed to be 2.019 and 1.921 Å, respectively. These bond metrics are

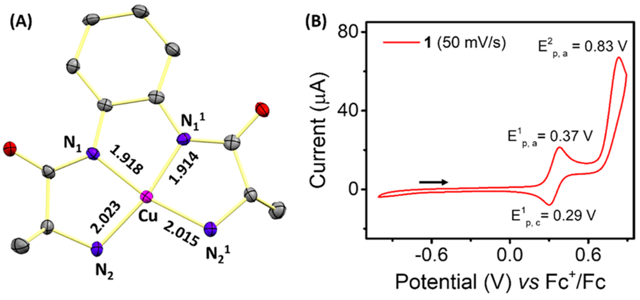

Figure 2. (A) X-ray crystal structure of **1** with 50% probability. Hydrogen atoms are omitted for clarity. Selected bond lengths are shown in the figure. CCDC 2343811. (B) Cyclic voltammogram of 2 mM **1** in MeOH at 25 °C with a scan rate of 50 mV/s.

consistent with those observed in Cu(II) complexes with similar ligands.[18,19] The Cu−N_{amide} bond distance is 0.1 Å shorter than the Cu−N_{amine} bond distance. This difference is attributed to the anionic coordination of the deprotonated N_{amide} donor instead of the neutral N_{amine} group.

1 exhibits a weak d-d absorption band at 500 nm ($\varepsilon_{500\ nm}$ = 240 M^{-1} cm^{-1}) in methanol (Figure S6). EPR spectrum of **1** shows an axial signal with $g_{//}$ = 2.04 and $g_{\perp}$ = 2.17, suggesting an S = 1/2 system, where the unpaired electron is mainly located in the d_{x2-y2} orbital of the Cu(II) center (Figure S7). ESI-MS analysis of **1** revealed signal at *m*/*z* 346.02, which can be formulated as $[(L)Cu(II)+(Cl)]^-$ (Figure S8). To explore the electrochemical properties of **1**, cyclic voltammetry (CV) analysis was conducted with various scan rates in CH_3OH. **1** manifested one quasi reversible redox waves at $E_{1/2}{}^1$ = 0.33 V vs Fc^+/Fc and an irreversible wave $E_{p,a}{}^2$ = 0.75 V vs Fc^+/Fc (Figures 2B and S9) at room temperature. The first redox wave at 0.33 V is assigned to the $(L^{\bullet +})$Cu(II)/(L)Cu(II) redox couple. The second oxidation event at 0.75 V vs Fc^+/Fc was assigned to the oxidation of the Cu(II) center (Table S2). To investigate whether the second redox event could be better resolved, cyclic voltammetry was conducted at 220 K. However, the voltammogram remained essentially unchanged at this temperature (Figure S10). Comparable redox behavior was also observed in aqueous solution at room temperature (Figure S11).

Treatment of **1** with aqueous NaOCl in methanol produces a blue-colored species with an absorption band at 598 nm at 25 °C. However, to achieve maximum absorbance, the addition of 15−20 equiv of NaOCl is required (Figure S12). According to the literature, NaOCl, in the presence of acid, significantly enhances the yield of reactive intermediates.[12] Taking this into account, **1** was treated with aqueous NaOCl and CH_3COOH in methanol. This reaction generates a metastable, blue-colored species **2**, with absorption bands at 580 nm ($\varepsilon_{580\ nm}$ = 2100 M^{-1} cm^{-1}) and 360 nm ($\varepsilon_{360\ nm}$ = 2600 M^{-1} cm^{-1}) over 60 s (Figure 3A). It was observed that the yield and formation rate of **2** depend on the concentrations of NaOCl and CH_3COOH. To attain the maximum yield of the 580 nm species (**2**), 3 equiv of NaOCl and 1 equiv of CH_3COOH are required. However, adding excess NaOCl decreases the yield of **2** (Figure S13). Various acids, including triflic acid, $HClO_4$, and HCl, were evaluated for their ability to promote the formation of **2**. In all cases, intermediate **2** was obtained in approximately 50% yield relative to that achieved with acetic acid. Among the acids tested, acetic acid was the most effective, affording **2** in the highest yield, and was therefore selected for all subsequent studies (Figure S14). Furthermore, we used chloramine-T as an oxidant to see if it could produce a species similar to that obtained with NaOCl. It is well established in the literature that chloramine-T produces the ClO^- when mixed with an acid.[20] Indeed, the reaction of **1** with 3 equiv of chloramine-T and 1 equiv of CH_3COOH resulted in the same blue-colored species, **2** (Figure S15). These experiments demonstrated that NaOCl and chloramine-T react with **1** in the presence of CH_3COOH to produce **2**. Additionally, when the solvent was changed from methanol to water, species **2** was generated, albeit at a lower yield (Figure S16). Therefore, the methanol and water solvent systems yield a common intermediate, **2**, likely constituting an OCl-derived copper complex. The possibility of -OMe/−OH/−OH_2 binding to the copper complex can be ruled out, or it is plausible that no ligand is coordinated axially (*vide infra*).

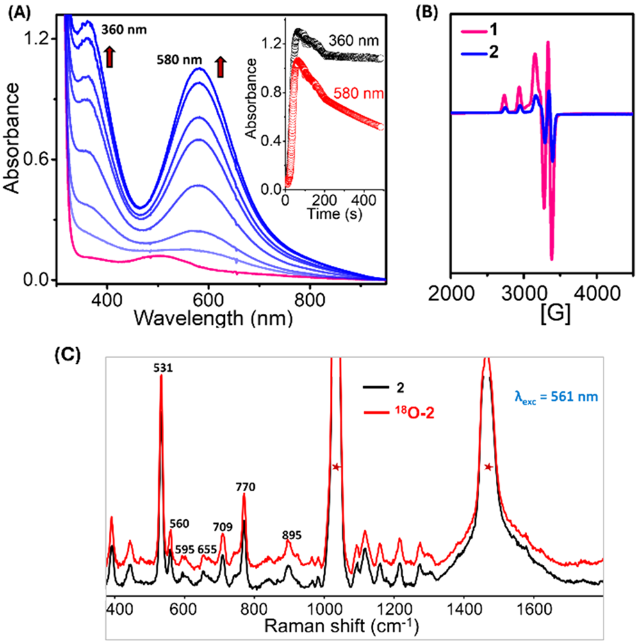

Figure 3. (A) UV/vis absorption changes upon the reaction of 0.5 mM **1** in methanol with 1 equiv of CH_3COOH and 3 equiv of aqueous NaOCl to form **2** at 25 °C. (inset) The corresponding absorbance changes at 580 nm (red trace) and 360 nm (blue trace) over time. (B) X-band EPR spectra of **1** (pink), and **2** (blue) obtained at its maximum formation in MeOH at 120 K. Modulation amplitude: 1.98 G; Modulation frequency: 100 kHz, and Attenuation: 18 dB. *Conditions to generate* **2**: *2 mM* **1** *in MeOH with 1 equiv of* CH_3COOH *and 3 equiv of NaOCl at 25 °C.* (C) Resonance Raman spectra of **2** generated in the reaction of 1 mM **1** and 1 equiv of CH_3COOH with 3 equiv of NaOCl (black) and $Na^{18}OCl$ (red) in MeOH at 25 °C, and the spectra were acquired at −60 °C. * Indicate the solvent bands.

To substantiate our conjecture regarding the intermediate being an OCl-derived complex, NaOBr was employed as an oxidant. The reaction of **1** with 3 equiv of NaOBr and 1 equiv of CH_3COOH yields an absorption band at 610 nm ($\varepsilon_{610\ nm}$ = 540 M^{-1} cm^{-1}) and a shoulder at 380 nm ($\varepsilon_{380\ nm}$ = 540 M^{-1} cm^{-1}) (Figure S17A). A 30 nm shift from 580 nm of **2** suggests an -OBr-derived copper intermediate in the latter case (Figure S17B). Additionally, it was observed that adding 3 equiv of NaOBr to **2** leads to the formation of the 610 nm absorbing species (Figure S18A), which indicates that OBr^- can replace ClO^-. However, the reaction of **1** with other oxo-transferring reagents, such as *m*CPBA and PhIO, does not yield **2** (Figure

S18B). The exclusive generation of **2** with NaOCl and chloramine-T in the presence of acetic acid underscores the indispensability of ClO^- to attain **2**.

The progression of the reaction leading to the formation of **2** was monitored by EPR spectroscopy. **1** displays an axial EPR signal with $g_{//} = 2.04$ and $g_{\perp} = 2.17$ indicative of an $S = 1/2$ Cu(II) system. Upon recording the EPR spectrum at the point of maximum accumulation of **2**, a notable decrease in the signal intensity of **1** was observed. Quantitative analysis of the EPR spins revealed that the system comprises 42% of the EPR active signal, corresponding to unreacted **1**, while the remaining 58% is EPR inactive (Figure 3B). These EPR inactive species could represent either a (L)Cu(III) or $(L^{\bullet+})$Cu(II). Although literature reports indicate that ligand frameworks incorporating a phenyl ring in the backbone can support metal-centered oxidation to Cu(III), in the present study, XAS analysis (*vide infra*) reveals that the oxidation is predominantly ligand-centered.[21,22]

The resonance Raman (rR) spectrum of **2** at excitation wavelength 561 nm shows several resonantly enhanced bands between 400 and 1400 cm^{-1}, among which two bands at 531 and 770 cm^{-1} are particularly intense (Figure 3C). However, none of these bands were shifted to a lower wavenumber upon employing $Na^{18}OCl$ as an oxidant. Hence, direct coordination of the ClO^- ligand with the copper center is less likely. The multiple bands in the rR spectrum originate from the ligand **L**. The 580 nm species generated with chloramine-T as an oxidant also gave the same rR spectrum (Figure S19). Furthermore, intermediate **2** was subjected to ESI-MS analysis, and a peak at *m/z* = 311.05 was observed, which could correspond to either the (L)Cu(III) or $(L^{\bullet+})$Cu(II) species (Figure S20).

From all the studies discussed thus far, it was clear that **2** is a one-electron oxidized species with a possible formulation as either (L)Cu(III) or $(L^{\bullet+})$Cu(II). Notably, the binding of OCl^- to the copper center in **2** is not evident, although ClO^- is essential for its generation. We studied the generation of a *formal* Cu(III) species using electron transfer oxidants such as ceric ammonium nitrate (CAN) and $[N(C_6H_3Br_2)_3^{\bullet}]^+$ (magic blue, MB) to verify whether intermediate **2** can be produced. The reaction of **1** with 1 equiv of CAN in MeOH at 25 °C produces a brown-colored species (**3**) with a distinct band at 485 nm ($\varepsilon_{485\ nm}$ = 2560 M^{-1} cm^{-1}) (Figures S21 and S22). The same species could be prepared using MB as an oxidant (Figures S21 and S22). Furthermore, **3** is prepared by bulk oxidation by applying 0.8 V vs Ag/AgCl to **1** in methanol, which produces the 485 nm species (Figures S21 and S22). At a maximum accumulation of **3** (generated using 1 equiv of CAN), the EPR signal intensity decreases significantly compared to **1**. The spin quantification reveals that 85% of the sample is EPR silent (Figure S23). ESI-MS analysis of **3** revealed once again a peak at *m/z* 311.05, attributed to either (L)Cu(III) or $(L^{\bullet+})$Cu(II) species (Figure S24). When the generated 485 nm (**3**) species react with 3 equiv of NaOCl, it produces a blue-color species with absorption bands at 515 and 360 nm. The band at 360 nm is distinct and appears only after the addition of NaOCl to **1**, implying that the generated species is **2**. However, in **2**, the second band is at 580 nm, not 515 nm. We reasoned that the 515 nm absorption band most likely comes from a mixture of 485 nm (*i.e.*, species **3**) and 580 nm (*i.e.*, species **2**) species in the solution (Figure S21B). The EPR analysis indicates that 80% of the EPR silent sample is present (Figure S25). The rR spectrum of the solution shows the same signals as those of species **2** generated by the reaction of **1** with NaOCl/chloramine-T and acetic acid (Figure S26). The identical rR spectra in both cases led us to propose OCl-derived copper species, *i.e.*, intermediate **2**.

X-ray absorption near edge structure (XANES) and extended X-ray absorption fine structure (EXAFS) analysis were further carried out on **1**, **2** (oxidized with NaOCl), and **3** (oxidized with CAN) to gain comparative insights into their coordination behaviors and structural conformations (Figure 4). The complexes were kept at 15 K in a He atmosphere at ambient pressure and recorded as fluorescence excitation spectra.

Cu K-edge XANES is generally characterized by a 1s → (4p +shakedown) transition[23] along the rising maximum edge between the pre-edge and white line, assigned as the 1s → 4p transition with concurrent ligand to metal charge transfer (LMCT), as illustrated in Figure 4A.[24] **1**, **2**, and **3** display the

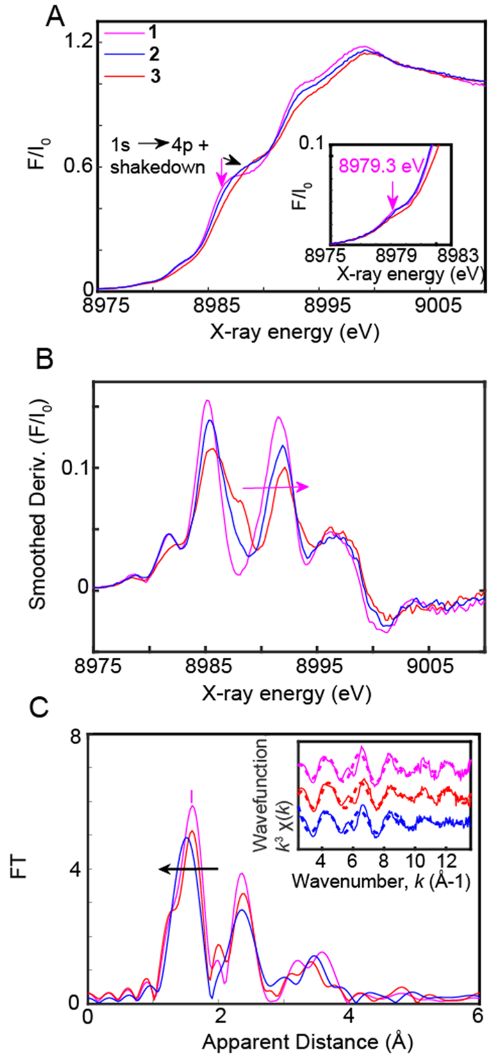

Figure 4. (A) Normalized Cu K-edge XANES spectra recorded at 15 K and Inset. Zoom-in of the pre-edge regions of **1** (pink), **2** (blue) and **3** (red) (B) Smoothed derivative of the Normalized Cu K-edge XANES spectra (C) Fourier transforms of k^3-weighted Cu EXAFS and $k^3[\chi(k)]$-weighted traces as a function of k, the photoelectron wave vector (solid lines) and fitted (dashed lines) of **1** (pink), **2** (blue) and **3** (red). Experimental spectra were calculated for k values of 2.469−13.596 $Å^{-1}$ (Figure 5C, inset).

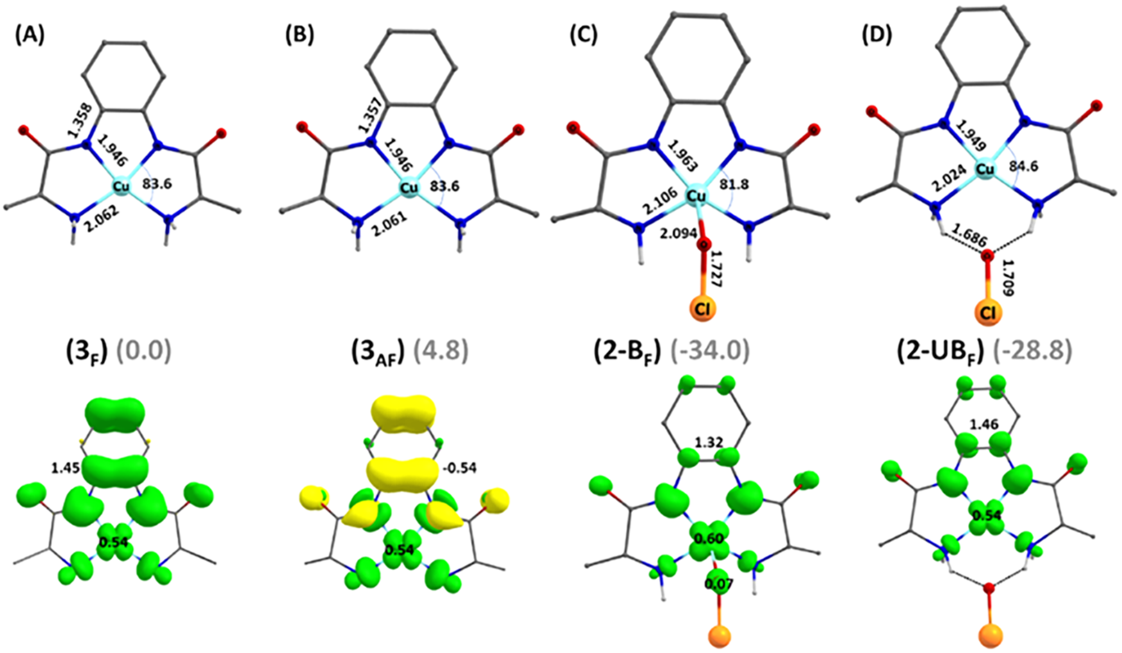

Figure 5. (Top) DFT optimized structures of (A) oxidized complex $\mathbf{3_F}$ (ferromagnetically coupled), (B) $\mathbf{3_{AF}}$ (antiferromagnetically coupled), (C) $\mathbf{2\text{-}B_F}$ (bound ferromagnetically coupled), (D) $\mathbf{2\text{-}UB_F}$ (unbound ferromagnetically coupled) showing important bond parameters (bond lengths in Å and angle in ∘) and values in parenthesis shows in energy values in kJ/mol. (Bottom) The respective spin density plot. Hydrogens attached to carbons are not shown for clarity.

1s → (4p + shakedown) peak at 8986.7 eV, 8987.8, and 8988.1 eV respectively. All three complexes exhibit the white line at 8988.8 eV and the conventional pre-edge 1s → 3d transition at 8979.3 eV, typical for Cu(II) complexes.[25c,26] The 1s → 3d transitions of Cu(II) and metal-oxidized Cu(III) complexes have been known to appear at ~8979 and ~8981 ± 0.5 eV[23] with a shift of ~1.5 to 2 eV. By contrast, in the event of a ligand-based oxidation process, the shift in the pre-edge energy has been known to be negligible or shifted by less than 1 eV.[26,27] The similar pre-edge features observed for all three complexes thus indicate a ligand-centered oxidation process in both **2** and **3**. Species **3** exhibits an energy shift of 0.8 eV from 8986.3 to 8987.1 eV. On the other hand, **2** oxidized with NaOCl exhibits a smaller energy shift of 0.3 eV, from 8986.3 to 8986.6 eV. The larger energy shift obtained in **3** vs **2** is consistent with the EPR quantification studies whereby a larger decrease in the EPR signal associated with 85% $(L^{\bullet+})$Cu(II) species being observed upon CAN addition vs only 58% of $(L^{\bullet+})$Cu(II) obtained by NaOCl oxidation (Figures 3B and S23).

The EXAFS spectra of all three complexes are further shown in Figure 4C, where a prominent peak (Peak **I**) is observed for **1**, **2**, and **3**, corresponding to the averaged Cu−N bond distances. The EXAFS fits are shown in Table S2, Figure 4C inset. EXAFS analysis of **1** revealed four Cu−N distances at 1.96 Å, which is the same as that derived from X-ray diffraction (XRD) analysis and within 0.02 Å of the averaged Cu−N distances of 2.00 Å, calculated through density functional theory (DFT) (Tables S3, Table S4, Fit 1).

By contrast, **3** showed four Cu−N distances of 1.96 Å as expected for a $(L^{\bullet+})$Cu(II) species (Table S3 Fit 4),[28] while **2** demonstrated more than twice the improvement of the overall fit quality with four vs five shortened Cu−N distances at 1.91 Å (Table S3, Fit 3 vs 2). The shortened Cu−N distances in **2** are probably consistent with a bound OCl in the secondary coordination sphere, which compacts its overall structure and decreases the average Cu−N distances. Furthermore, a better EXAFS fit quality was obtained for **2** with four Cu−N bond distances, which favors the formation of a -OCl unbound $(L^{\bullet+})$Cu(II) species and rules out a bound OCl to Cu, where the Cu−O distances would be expected to be ~2.09 Å (Figure 5). Importantly, the DFT optimization of $\mathbf{2\text{-}UB_F}$ (Figure 5) vs **1** shows a decrease in the average Cu−N bond distances consistent with experimental EXAFS fits. Combined experimental XANES and EXAFS analysis thus supports the formation of -OCl unbound $(L^{\bullet+})$Cu(II) and $(L^{\bullet+})$Cu(II) species in **2** and **3**, respectively, in agreement with previously elaborated experimental findings and computational studies (*vide infra*).

To understand the electronic structure of complexes **1** and **3**, we performed DFT calculations (B3LYP-D3/TZVP). The optimized geometry of **1** (Figure S27 and Table S4) is consistent with the crystal structure. The computed spin density plot of **1** reveals that the unpaired electron is mainly located in the $d_{x^2-y^2}$ orbital, with 54% spin density at the Cu(II) center and the remainder delocalized to the coordinated nitrogen atoms. This finding is consistent with the electronic structure description elucidated from the EPR spectroscopy. We have also computed the magnetic anisotropy in **1** using CASSCF calculations, which suggest the $g_{\parallel}$ and $g_{\perp}$ values of 2.06 and 2.26, respectively, as the unpaired electron resides primarily in the XY plane ($d_{x^2-y^2}$ orbital). These computed values are in close agreement with the experimental values. The eigenvalue plot of **1** indicates a strong antibonding character for the $d_{x^2-y^2}$ orbital, which is significantly destabilized compared to the d_z^2 orbital by 2.81 eV (Figure S28). The $d_{x^2-y^2}$ orbital, due to strong Cu(II)-ligand covalency, is strongly delocalized, with significant contributions to this molecular orbital (MO) from the ligand framework. Thus, although destabilizing, the $d_{x^2-y^2}$ orbital favors the formation of

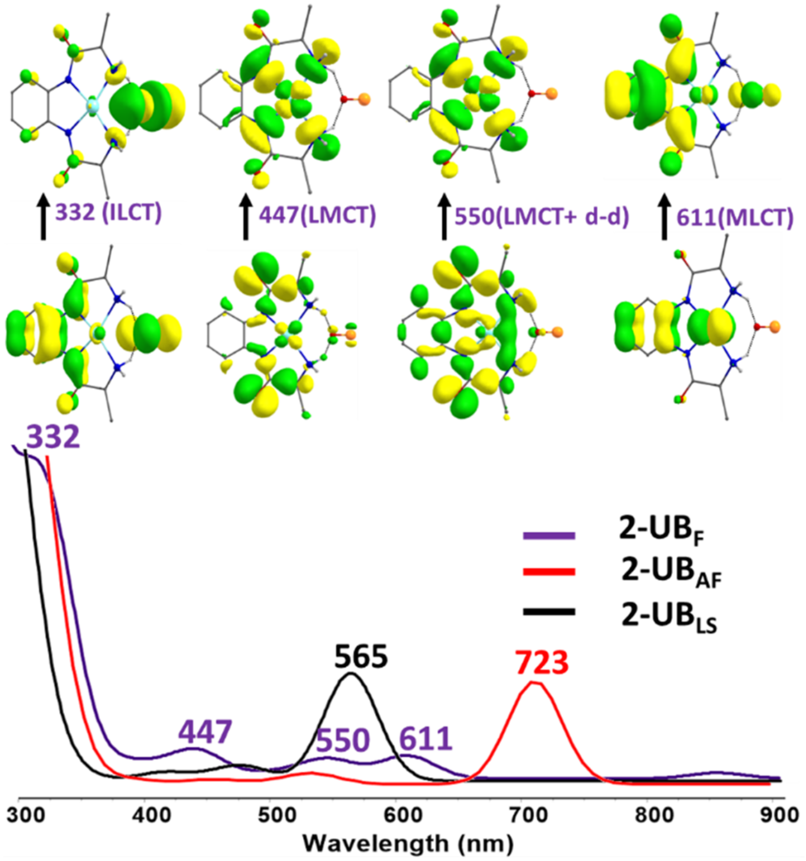

Figure 6. Electronic absorption spectra of complex **2-UB** with all possible spin states. The respective transition/orbitals corresponding to the peaks of the ferromagnetically coupled ground state (**2-UB**$_{\mathbf{F}}$) were shown at the top.

Cu(III), and strong delocalization suggests a possible reduction in the ligand moiety. A strongly localized $d_{x^2-y^2}$ orbital is expected to produce a *formal* Cu(III) species. Furthermore, HOMO of **1** is found to be a π^* orbital of the phenyl moiety (Figure S29), suggesting that further oxidation in **1** is expected to be ligand centric.

We then considered the one-electron oxidized species of **1** (*i.e.*, **3**) and evaluated the geometries of (i) a *formal* Cu(III) species with net zero spin density at the Cu center ($\mathbf{3_{LS}}$), (ii) a $(L^{\bullet+})$Cu(II) species in a triplet state where there is ferromagnetic coupling between the Cu(II) center and the radical located at the ligand ($\mathbf{3_F}$), and (iii) a singlet state with $(L^{\bullet})$Cu(II) with antiferromagnetic coupling ($\mathbf{3_{AF}}$). The optimized geometries reveal that the bond lengths in all three cases are slightly shorter than **1**, with $\mathbf{3_{LS}}$ (Figure S30) exhibiting longer Cu-ligand bond lengths compared to $\mathbf{3_F}$ and $\mathbf{3_{AF}}$ (Figure 5A, B, top). The spin density at the Cu centers in $\mathbf{3_F}$ and $\mathbf{3_{AF}}$ was found to be strongly delocalized (0.54 at the Cu center), with the rest of the spin density located on the ligand moiety. The unpaired electron on the ligand moiety is located in the π^* orbital of the phenyl ring, which is oriented perpendicular to the plane (Figure 5A, B, bottom). As a result, there is minimal overlap between the $d_{x^2-y^2}$ orbital of copper and the $\pi^*\ L^{\bullet}$ orbital. This minimal overlap is reflected in the computed energy levels: the $\mathbf{3_F}$ state ($S = 1$) is the ground state, the $\mathbf{3_{AF}}$ state lies 4.8 kJ/mol higher, and the Cu(III) state ($\mathbf{3_{LS}}$) is significantly higher at 44.7 kJ/mol.

Thus, DFT calculations predict $(L^{\bullet+})$Cu(II) as the electronic structure of species **3**, with the ferromagnetic coupling between the two paramagnetic centers. As an integer-spin ground state with expected zero-field splitting, this species is expected to be EPR silent at the X-band frequency, as observed in the experiments. Both $\mathbf{3_{LS}}$ and $\mathbf{3_{AF}}$, being diamagnetic, are expected to be EPR silent as well. Therefore, EPR experiments cannot rule out either of these possibilities. To further affirm the nature of the ground state, we computed the absorption feature of the $\mathbf{3_{LS}}$, $\mathbf{3_F}$, and $\mathbf{3_{AF}}$ species using TD-DFT methods (see computational details for more information). When comparing the computed absorption features of all three species, the major ones are reproduced well for the $\mathbf{3_F}$ species compared to the other two, reiterating that $\mathbf{3_F}$ is the ground state. Notably, the peak at 492 nm (λ_{exp} = 485 nm) observed corresponds to π^*(C−O)-ligand to $d_{x^2-y^2}$ (Cu) charge transfer transition (Figure S31), and the peak at 603 nm (d_{xy} to $d_{x^2-y^2}$ in Figure S31) corresponds to a d-d transition. These features are consistent with the experimental observations.

Further, we examined the geometry and electronic structure of species **2**. Here, two possibilities were considered: one with OCl bound to the Cu center (**2-B**) and the other where -OCl is anchored to the ligand via noncovalent interactions (**2-UB**). We considered three different possible states Cu(III) and $(L^{\bullet+})$Cu(II) leading to the following six combinations: $\mathbf{2\text{-}B_F}$, $\mathbf{2\text{-}UB_F}$, $\mathbf{2\text{-}UB_{LS}}$, $\mathbf{2\text{-}B_{AF}}$, $\mathbf{2\text{-}UB_{AF}}$, and $\mathbf{2\text{-}B_{LS}}$, with the estimated energy of 0.0 kJ/mol, 5.2 kJ/mol, 6.5 kJ/mol, 8.6, 9.6, and 58 kJ/mol, respectively. The optimized geometries of these states/species are given in Figure 5C and 5D ($\mathbf{2\text{-}B_F}$ and $\mathbf{2\text{-}UB_F}$) and Figures S32 and S33.

For the unbound species, the -OCl group was anchored by H-bonding interactions with the NH_2 groups present in the

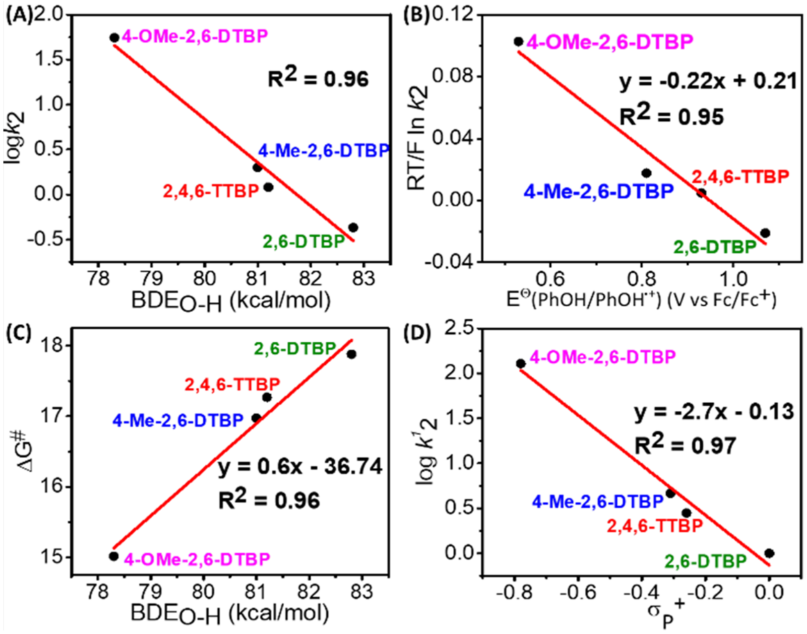

Figure 7. (A) BDE Plot for **2**: Bond dissociation energy of various phenols vs logk_2. (B) Marcus Plot for **2**: Redox potential of various phenols vs (RT/F) lnk_2. (C) Bell-Evans Polanyi Plot for **2**: Bond dissociation energy of various phenols vs Gibbs Energy ($\Delta G^{\ddagger}$). (D) Hammett Plot for **2**: Substitution constant of various para-substituted phenols vs logk_2.

ligand moiety. Computed energies reveal that the bound -OCl with an S = 1 state having a (L$^{\bullet+}$)Cu(II) electronic structure is the ground state, with the unbound -OCl being only marginally higher in energy, with other species lying within 10 kJ/mol (except for **2-B$_{\mathrm{LS}}$**). Considering this small energy gap and the expected errors in the DFT calculations,[29,30] it is hard to distinguish the nature of the ground state from these calculations. We calculated the formation energy of these states from species **3**. The formation of **2-B$_{\mathrm{F}}$** was found to be exothermic by 34.0 kJ/mol, while all other states, except **2-B$_{\mathrm{LS}}$** (+24 kJ/mol), were also found to be exothermic and did not help to discriminate among them. Therefore, we turned to absorption features employing TD-DFT to identify the species. The absorption spectra of the bound -OCl species (**2-B$_{\mathrm{F}}$**) (Figure S34) reveal 306 and 526 nm features attributed to d-d transitions and intraligand charge transfer, respectively. Additionally, our calculations reveal a high-intensity peak at 811 nm, indicative of intravalence charge transfer (IVCT). This peak corresponds to charge transfer from the Cu center to ligand orbitals, including that of -OCl MOs, suggesting a (L$^{\bullet+}$)Cu(II)-OCl to (L)Cu(III)-OCl transition. Interestingly, this peak is absent in the experiments. Even careful scanning of this region yielded no peak at this wavelength. Therefore, we suggest that bound -OCl is unlikely to be the ground state structure. Furthermore, Figure 6 illustrates the absorption spectra of the **2-UB$_{\mathrm{F}}$**, where all major absorption features observed in experiments are reproduced in the calculations.

Particularly noteworthy is a peak at 332 nm, indicative of intraligand charge transfer (ILCT) (as depicted in Figure S28), and the peak observed at 550 nm, corresponding to the LMCT transition from π^* of the ligand with some contribution from d_{xy} orbital to dominantly d_{x-y}^{22} orbital, rationalizing the large ε experimental value. These correspond to the peaks observed at 360 and 580 nm in the experiments. Interestingly, for the -OCl unbound species, the IVCT band in the near-IR region is absent, suggesting that this is likely the ground state observed in the experiments.

Moreover, a normalized TD-DFT XANES simulation was performed to validate our findings. For **3**, the calculated values for **3$_{\mathrm{AF}}$** and **3$_{\mathrm{F}}$** are 8989.4 and 8988 eV, respectively, aligning with the experimental observations (8988.1 eV). Similarly, for **2**, the experimental peak at 8987.8 eV closely matches the calculated value of 8987.5 eV for the unbound species (**2-UB$_{\mathrm{F}}$**), further supporting its identification as the ground state (Figure S35).

The oxidizing ability of **2** was assessed using 4-substituted 2,6-di*tert*-butyl phenols (4-X-2,6-DTBP, X = OMe, ^{t}Bu, Me, and H). The reactions were carried out under pseudo-first order conditions, [**2**] ≪ [phenol derivatives]. It is observed that reaction rates (k_{obs}) increase linearly with increasing phenolic substrate concentration, giving the second-order rate constant k_2 (Figures S36−S39). The bond dissociation plot (BDE) of BDE$_{\mathrm{O-H}}$ vs logk_2 shows that decreasing the O−H bond strength leads to an increase in the reaction rate and *vice versa* (Figure 7A). The observed reaction rates (k_2) for intermediate **2** are relatively lower compared to the reported Cu(III) intermediates (Table S5). We performed a Marcus plot analysis to determine the pathway via which these phenols are oxidized. It is a plot between (RT/F) lnk_2 vs $E^\circ{}_{(\mathrm{PhOH/PhO}^{\bullet+})}$ where k_2 is the second-order rate constant for the reaction and E° is the redox potential for 4-X-2,6-DTBP. Depending on the slope, the Marcus plot predicts various mechanistic pathways in the rate-determining step. The slope of approximately −1.0 indicates proton transfer in the rate-determining step, while the slope of −0.5 indicates single electron transfer, and a value near zero indicates a hydrogen atom transfer mechanism. The plot of (RT/F) ln k_2 vs $E^\circ{}_{(\mathrm{PhOH/PhO}^{\bullet+})}$ shows a slope of around −0.22, close to zero (Figure 7B), indicating that the reaction follows the HAA pathway.[31]

A Bell-Evans Polanyi plot was obtained by plotting $\Delta G^{\ddagger}$ vs BDE$_{\mathrm{O-H}}$, where $\Delta G^{\ddagger}$ is the Gibbs free energy of activation calculated from k_2 values, and BDE$_{\mathrm{O-H}}$ is the strength of the O−H bond in phenols. The slope of 0.60 indicates that the reaction between **2** and 4-X-2,6-DTBP involves a hydrogen atom transfer (HAT) process (Figure 7C). Theoretically, the value for the HAT reaction is 0.5. Hammett analysis revealed a negative slope supporting the hydrogen atom transfer reaction mechanism (Figure 7D).[32−34] All the above studies suggest that the reaction between **2** and 4-X-2,6-DTBP proceeds through HAT.

To further probe the reaction mechanism, two sterically distinct but electronically similar substrates, 2,6-di-*tert*-butylphenol (2,6-DTBP) and 2,4-di-*tert*-butylphenol (2,4-DTBP), were employed. Both substrates possess comparable O−H bond dissociation energies and similar pK_a values (2,6-DTBP: pK_a = 11.70; 2,4-DTBP: pK_a = 11.64). Given that the primary difference lies in their steric profiles, a proton-coupled electron transfer (PCET) mechanism would be expected to yield comparable reaction rates (Figure S40).[35] However, the reaction rate of **2** with 2,4-DTBP was determined to be 9.2 M^{-1} s^{-1}, approximately 15-fold higher than that observed with 2,6-DTBP. This pronounced rate difference supports the HAA mechanism, wherein steric hindrance significantly influences reactivity toward trisubstituted phenols.

The reaction of trisubstituted phenols with high-valent copper intermediates produces a metastable phenoxyl radical that can be detected using UV−vis absorption spectroscopy. Treatment with 2,6-DTBP results in a band at 420 nm at the expense of a 580 nm band due to **2**. The generated 420 nm is typical for DPQ (DPQ = 3,3′,5,5′-tetra-tert-butyldiphenoquinone) with 25% yield (Figures S41, S42A and Table S6). The formation of DPQ occurs via the initial formation of 2,6-DTBP$^{\bullet+}$, and subsequent coupling of these radicals produces DPQ (Scheme S2). The reaction of **2** with 4-OMe-2,6-DTBP shows an absorption band at 408 nm, characteristic of 4-OMe-2,6-DTBP$^{\bullet+}$ species (Figure S42B). These radicals are further coupled to give 2,6-di-*tert*-butyl-1,4-benzoquinone (BQ) with 75% yield (Figure S43, Table S6, and Scheme S3). The addition of 2,4,6-TTBP to **2** gave rise to an absorption band at 403 nm with sudden decay at 580 nm. The 403 nm absorption band is characteristic of 2,4,6-TTBP$^{\bullet+}$ species (Figure S42C).[33] Furthermore, EPR analysis of the decayed species obtained after the reaction of **2** with 2,6-DTBP revealed an axial signal that closely matches the spectrum of the initial Cu(II) complex (**1**), indicating reversion to the Cu(II) state upon the reaction (Figure S44). Blank reactions between trisubstituted phenols and NaOCl/CH_3COOH give minimal background reaction within the catalytic time (Figure S42). These control experiments suggest that **2** is responsible for the observed reactivity.

To further compare the reactivity of intermediates **2** and **3**, they were examined in the resence of trisubstituted phenols. Species **3** was found to react more rapidly than **2**, as summarized in Table 1 and Figure S45. The interaction of OCl^- in the secondary coordination sphere appears to diminish the electrophilicity of the Cu center, leading to reduced reaction rates. The origin of the enhanced reactivity of **3** relative to **2** remains to be elucidated.

Table 1. Second-Order Rate Constants for 2 and 3 with Various Trisubstituted Phenols

substrate	k_2 (M^{-1} s^{-1}) (2)	k_2 (M^{-1} s^{-1}) (3)	BDE ($kcalmol^{-1}$)[31]	$E_{1/2}$ (vs Fc$^{0/+}$)[31]
4-OMe-2,6-DTBP	55.3	154.8	78.3	0.53
4-Me-2,6-DTBP	2	38.9	81.0	0.81
2,4,6-TTBP	1.21	12.02	81.2	0.93
2,6-DTBP	0.43	6.16	82.8	1.07

The intermediate **2** is generated through two different pathways: (i) by reacting **1** with NaOCl/chloramine-T in the presence of CH_3COOH, and (ii) by initially generating **3** through the reaction of **1** with CAN, followed by treatment with NaOCl to yield a similar intermediate **2**. As illustrated in Scheme 1, it is clear that the presence of ClO^- is essential for generating **2**. To the decayed species of **2**, the addition of CH_3COOH and NaOCl regenerated species **2** to the same extent, further supporting the structural integrity of the ligand (Figure S46). This study presents the first example of ClO^- stabilization through hydrogen bonding interactions with high-valent metal intermediates, mimicking the mechanism of flavin-dependent halogenase enzymes. Additionally, **2** can undergo HAA reactions with trisubstituted phenols.

CONCLUSIONS

Inspired by flavin-dependent halogenases, where HOCl is hydrogen bonded to the K79 residue of the enzyme, we propose a *formal* Cu(III) complex ligated with the OPDAla framework and exhibiting a hydrogen bonding interaction with hypochlorite in this study. The intermediates **2** and **3** were characterized using various spectroscopic and spectrometric methods, including UV/vis absorption, EPR, rR, ESI-MS, XANES, and EXAFS. Resonance Raman spectroscopy and EXAFS analysis of **2** revealed that hypochlorite is not directly bound to the copper center. Additionally, extensive DFT calculations support the hydrogen bonding interaction of hypochlorite with the *formal* Cu(III) complex. Moreover, intermediate **2** can perform HAA reactions with various trisubstituted phenols. To the best of our knowledge, this work is the first example of such a species in which hypochlorite is linked to the secondary coordination sphere rather than directly coordinating with the metal center. This study is a new discovery and could pave the way for developing the next generation of complexes mimicking the previously under-explored flavin-dependent halogenases.

EXPERIMENTAL SECTION

All chemicals and reagents were obtained from commercial sources and were used as received. HPLC grade H_2O and CH_3OH from Merck were used in spectroscopic studies. An Agilent 8453 diode-array spectrophotometer was used to record UV/vis absorption spectra and conduct kinetic experiments spectrophotometrically using 1 cm quartz cells (λ = 200−1000 nm range). ESI-MS was recorded on an Agilent 6546 LC/Q-TOF instrument in the positive and negative ion modes. A Bruker EMX 1444 spectrometer with a temperature controller was employed to record the X-band EPR data at 120 K. Simulation of the EPR spectrum of **1** was carried out using Bruker WINEPR SimFonia software. ^{1}H NMR spectra were obtained using JEOL JNM LA 500 (500 MHz) and JEOL JNM LA 400 (400 MHz) NMR spectrometers. Cyclic voltammetry experiments were carried out at room temperature using a CH Instruments Electrochemical Analyzer M-600B series. A three-electrode system was used where a glassy carbon was used as a working electrode, a Pt wire was used as an auxiliary electrode, and the aqueous Ag/AgCl (3 M aq. KCl solution) was used the reference electrode. 100 mM of KNO_3 in water and tetra-*n*-butylammonium perchlorate in methanol were used as a supporting electrolyte. Resonance Raman spectra of **2** were obtained at 638 nm (80 mW, Cobolt lasers, HÜBNER Photonics) and 561 nm (100 mW, Cobolt lasers, HÜBNER Photonics) excitation wavelengths using a Kymera 328i motorized Czerny-Turner spectrograph (Andor Technology) equipped with a DU 420A-BEX2-DD camera

Scheme 1. Generation of Intermediate 2 via Different Pathways and Its Reactivity

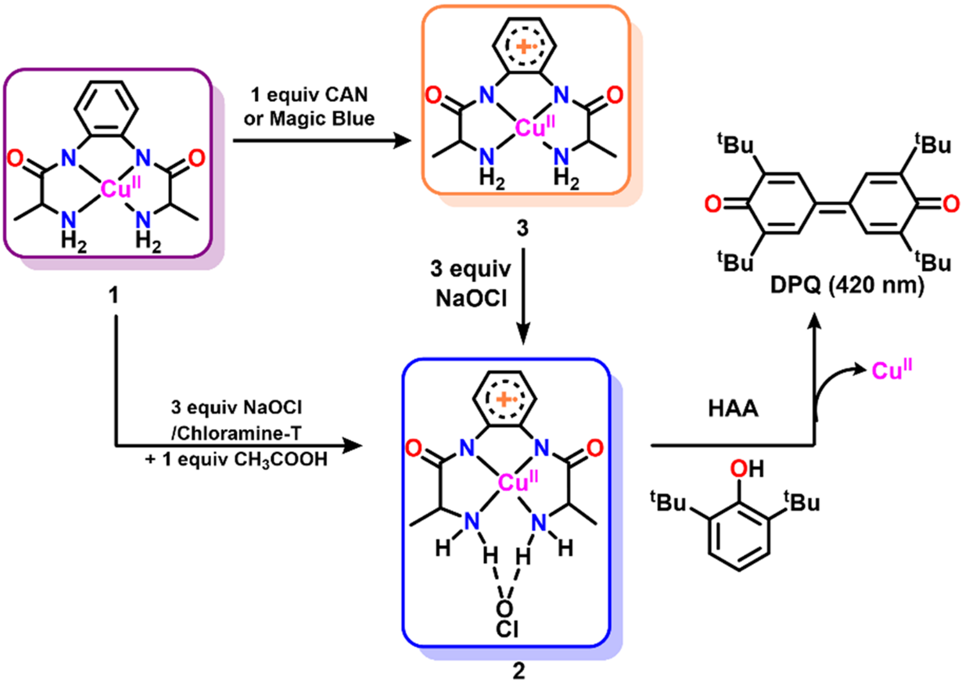

(iDus 420 CCD, Andor Technology). The CCD camera was cooled to −80 °C. The spectral slit width of the instrument was set to 100 μm. The spectral calibration was performed using a 1:1 CH_3CN:toluene (v/v) solvent mixture.

X-ray Crystallography. A single crystal of suitable dimensions was used for data collection. Diffraction intensities were collected on a Bruker APEX-II CCD diffractometer with graphite-monochromated Mo Kα (0.71073 Å) radiation at 100(2) K. Data were corrected for Lorentz and polarization effects; empirical absorption corrections (SADABS v 2.10) were applied. Using Olex2,[36] the structures were solved using the ShelXT26 structure solution program with intrinsic phasing and refined with the ShelXL[37] refinement package using least-squares minimization. The non-hydrogen atoms were refined anisotropically, whereas the H atoms fixed to their geometrically ideal positions were refined isotropically. All non-hydrogen atoms were refined with anisotropic thermal parameters by full-matrix least-squares procedures on F^2. CCDC 2343811 includes the supplementary crystallographic data for **1**.

Steady-State XAS in the Solution. The X-ray absorption spectra of the solution samples of **1**, **2**, and **3** of the monomer, dimer, and trimer were collected at the P65 beamline at DESY (Germany) on the mini-undulator beamline at electron energy 8.998 keV and an average current of 100 mA. The radiation was monochromatized by a Si(111) crystal monochromator. The intensity of the X-rays was monitored by three ion chambers (I_0, I_1, and I_2). I_0, placed before the sample, was filled with 92% nitrogen and 8% argon. I_1 and I_2 were placed after the sample. I_1 was filled with 86% N_2 and 14% Ar, while I_2 was filled with 100% Kr. Cu metal was placed between ion chambers I_1 and I_2, and its absorption was recorded with each scan for energy calibration. Cu XAS energy was calibrated by the first maxima in the second derivative of the Copper's metal foil's X-ray absorption near edge structure (XANES) spectrum. The samples were kept at 5 K in a He atmosphere at ambient pressure and recorded as fluorescence excitation spectra using a 4-element energy-resolving Silicon drift detector. The solution complexes were measured in the continuous helium flow cryostat in fluorescence mode. Around 5−10 XAS spectra of each sample were collected. Care was taken to measure at several sample positions on each sample, and no more than 5 scans were taken at each sample position. In order to reduce the risk of sample damage by X-ray radiation, 80% flux was used (beam size 2300 μm(Horizontal) × 300 μm(Vertical)), and no damage was observed scan after scan to any samples. Cu XAS energy was calibrated by the first maxima in the second derivative of the Copper's metal X-ray Absorption Near Edge Structure (XANES) spectrum.

Extended X-ray Absorption Fine Structure (EXAFS) Analysis. Athena software[38] was used for data processing. The energy scale for each scan was normalized using the copper metal standard.[39] Data in energy space were pre-edge corrected, normalized, deglitched (if necessary), $k = [2m(E-E_0)/\hbar^2]^{1/2}$ and background corrected. The processed data were next converted to the photoelectron wave vector (k) space and weighted by k. The electron wavenumber is defined as, E_0 is the energy origin or the threshold energy. K-space data were truncated near the zero crossings k = 2.469 to 13.596 Å^{-1} in Cu EXAFS before Fourier transformation. The k-space data were transferred into the Artemis Software for curve fitting. To fit the data, the Fourier peaks were isolated separately, and grouped, or the entire (unfiltered) spectrum was used. The individual Fourier peaks were isolated by applying a Hanning window to the first and last 15% of the chosen range, leaving the middle 70% untouched. Curve fitting was performed using *ab initio*-calculated phases and amplitudes from the FEFF8[23] program at the University of Washington. *Ab initio*-calculated phases and amplitudes were used in the EXAFS eq S1.

$$\chi(k) = S_0^2 \sum_j \frac{N_j}{kR_j^2} f_{\mathrm{eff}_j}(\pi, k, R_j) e^{-2\sigma_j^2 k^2} e^{-2R_j/\lambda_j(k)} \sin(2kR_j + \phi_{ij}(k)) \tag{S1}$$

Where N_j is the number of atoms in the jth shell; R_j is the mean distance between the absorbing $e^{-2\sigma_j^2k^2}$ atom and the atoms in the jth f_{eff_j} shell; (p,k,R_j) is the *ab initio* amplitude function for shell j, and the Debye−Waller term accounts for damping due to static and thermal disorder in absorber-backscattered distances. The mean free path term $e^{-2R_j/\lambda_j(k)}$ reflects losses due to inelastic scattering, where $\lambda_j(k)$, is the electron mean free path. The oscillations in the EXAFS spectrum are reflected in the sinusoidal term, where $\phi_{ij}(k)$ is the *ab initio* phase function for shell j. This sinusoidal term shows the direct relation $\sin(2kR_j + \phi_{ij}(k))$ between the frequency of the EXAFS oscillations in k-space and the absorber-backscatterer distance. $S_0{}^2$ is an amplitude reduction factor.

The EXAFS equation[35] (eq S1) was used to fit the experimental Fourier isolated data (q-space) as well as unfiltered data (k-space) and

Fourier transformed data (R-space) using N, S_0^2, E_0, R, and σ^2 as variable parameters. N refers to the number of coordination atoms surrounding Cu for each shell. The quality of fit was evaluated by the R-factor (eq S2) and the reduced Chi^2 value. The deviation in E_0 ought to be less than or equal to 10 eV. R-factor less than 2% denotes that the fit is good enough[5] whereas R-factor between 2 and 5% denotes that the fit is correct within a consistently broad model. The reduced Chi^2 value is used to compare fits as more absorber-backscatter shells are included to fit the data. A smaller reduced Chi^2 value implies a better fit. Similar results were obtained from fits done in k, q, and R-spaces.

$$R\text{-factor} = \frac{\sum_i (\text{difference between data and fit}_i)^2}{\sum_i (\text{data})^2} \tag{S2}$$

Computational Details. Unrestrained geometry optimization of **1** was carried out employing the density functional theory (DFT) method using the Gaussian 16 suite of program.[40] The crystal structure of the catalyst was considered as the starting coordinates for the geometry optimizations. A dispersion-corrected unrestricted B3LYP-D2 hybrid density functional has been employed.[41,42] A TZVP basis set is employed for all the atoms for optimization. Solvation effects were considered through the Polarizable Continuum Model (PCM)[43] with Methanol as the solvent. To validate our computational methods, we compared the optimized structures of **1** with single-crystal X-ray diffraction data, revealing good agreement (as depicted in Table S2).

All optimized geometries correspond to the global minima in their respective spin surfaces and are indicated by all of the positive frequencies from the harmonic vibrational frequency calculations on the optimized geometries at 298.15 K. The final quoted energies are the Gibbs free energy-corrected electronic energies. The natural bonding orbital (NBO) and spin natural orbital (SNO) analyses implemented in the Gaussian 16 program were performed to find the bonding patterns, orbital occupancy, and spin densities. The optimized geometries and spin densities were visualized using the Chemcraft version 1.8.[44]

The ORCA package was used to calculate the absorption spectra and TDDFT XANES. Time-dependent density functional theory (TDDFT) implemented in the ORCA program was used for the calculation of excitation energies. The Time-dependent (TD) DFT method has been used to obtain these electronic transitions for complexes. TDDFT calculations have been performed by using BP86 functional along with the TZVP basis set for all atoms. The RIJCOSX approximation with def2/J auxiliary basis set has been employed. The Conductor-like Polarizable Continuum Model (CPCM) has been utilized to incorporate solvent effects, with a dielectric constant of 32.7 corresponding to methanol solvent. For XANES, we have used the same functionals and basis sets and normalized the peaks by 19.5 eV to match the experimental values.

Synthesis of N,N′-(1,2-Phenylene)bis(2-aminopropanamide) (H_2L) and Complex 1. Step 1: In a round-bottom (RB) flask, N-carbobenzyloxy-L-alanine (500 mg, 2.2 mmol) was dissolved in DCM and the solution was cooled to 0 °C. To this precooled solution, EDC·HCl (518 mg, 2.70 mmol) and HoBt (365 mg, 2.70 mmol) were added sequentially, and the reaction was allowed to stir at 0 °C for 20 min. After 20 min, $NaHCO_3$ (848 mg, 10 mmol) and orthophenylenediamine (121 mg, 1.12 mmol) were added at the same temperature. The reaction mixture was stirred at room temperature for the next 24 h. Reaction completion was monitored by TLC using a 1:1 (ethyl acetate/hexane) solvent system with R_f = 0.35. Upon completion of the reaction, 30 mL of water was added, and the mixture was extracted with CH_2Cl_2 (3 × 30 mL). The organic layer was washed with sat. $NaHCO_3$ (30 mL), 1 N aq. HCl (30 mL) and brine (2 × 30 mL). The organic layer was dried over anhydrous Na_2SO_4. The organic solvent was evaporated under reduced pressure to obtain an off-white solid, which was further washed with ether to give a white solid with a 60% yield. ^{1}H NMR (500 MHz, DMSO-d_6): δ (ppm) 9.31 (s), 7.59 (d, J 6.4), 7.51 (d, J 3.4), 7.36–7.24 (m), 7.14 (dd, J 5.7, 3.6), 5.01 (dd, J 36.1, 12.5), 4.25–4.15 (m), 1.28 (d, J 7.1) (Figure S33). ^{13}C NMR (126 MHz, DMSO-d_6): δ (ppm) 172.27, 156.54, 137.39, 131.02, 128.87, 128.35, 125.78, 125.18, 66.16, 51.37, 18.26 (Figure S34).

Step 2: 200 mg of the solid obtained in step 1 was dissolved in dry methanol (10 mL). To this solution, 10% Pd/C was added under a hydrogen atmosphere and stirred for 8–10 h. After this period, the solution was filtered through filter paper, and the solvent was removed under reduced pressure to give a pure white solid of ligand (**L**) with a 50% yield. ^{1}H NMR (400 MHz, DMSO-d_6): δ (ppm) 7.58–7.52 (m, 1H), 7.13–7.07 (m, 1H), 3.40 (q, J = 6.9 Hz, 1H), 1.21 (d, J = 6.9 Hz, 3H) (Figure S35). ^{13}C NMR (100 MHz, DMSO-d_6): δ (ppm) 175.44, 131.12, 125.42, 124.67, 51.40, 21.83 (Figure S36).

Synthesis of 1. Synthesis of **1** was adopted from a literature report.[45] A 5 mL methanolic solution of ligand (100 mg, 0.4 mmol) was added to a methanolic solution of $Cu^{II}(OAc)_2\cdot H_2O$ (80 mg, 0.4 mmol, 5 mL). The color of the solution turned blue. The reaction was allowed to stir at room temperature for 30 min, after which 1 M methanolic KOH (44.8 mg, 0.85 mmol, 0.8 mL) was added, causing the color of the solution to change from blue to purple. The reaction was further stirred at room temperature overnight. The solvent was removed to half of its initial volume under reduced pressure, and ether was added to the reaction mixture, immediately forming a purple precipitate. The solution was filtered, and the crude product was collected with a 40% yield. The crystals were grown by dissolving the crude product in methanol and allowing ether vapor diffusion, resulting in purple crystals of **1** in 3–4 days at 10 °C. UV/vis absorption: 500 nm (240 M^{-1} cm^{-1} in MeOH). ESI-MS: $[LCu(II)+Cl]^-$ m/z = 346.02. EPR: $g_{\parallel}$ = 2.04 and $g_{\perp}$ = 2.17 in MeOH at 120 K. Anal. Calc. for $CuC_{12}H_{16}N_4O_2$: C, 46.22; N, 17.93; H, 5.17. Found: C, 46.23; N, 17.83; H, 5.504.

Preparation of NaOBr. In a glass vial, 450 μL of a 1.93 M aqueous NaOCl solution was taken, and 223 mg (2.5 equiv) of solid NaBr was added. The reaction mixture was stirred at room temperature for 5 min, resulting in a pale-yellow solution of NaOBr with a concentration of 1.93 M.

■ ASSOCIATED CONTENT

Data Availability Statement

Other data presented here is available in the Supporting Information.

Supporting Information

The Supporting Information is available free of charge at https://pubs.acs.org/doi/10.1021/acs.inorgchem.5c01273.

UV/vis absorption, EPR spectroscopy, Raman spectroscopy, k_2 plots, and DFT calculations (PDF)

Accession Codes

Deposition Number 2343811 contains the supplementary crystallographic data for this paper. These data can be obtained free of charge via the joint Cambridge Crystallographic Data Center (CCDC) and Fachinformationszentrum Karlsruhe Access Structures service.

■ AUTHOR INFORMATION

Corresponding Authors

Dooshaye Moonshiram – *Instituto de Ciencia de Materiales de Madrid, Consejo Superior de Investigaciones Cienti′ficas, 28049 Madrid, Spain;* orcid.org/0000-0002-9075-3035; Email: dooshaye.moonshiram@csic.es

Gopalan Rajaraman – *Department of Chemistry, Indian Institute of Technology Bombay, Mumbai 400076, India;* orcid.org/0000-0001-6133-3026; Email: rajaraman@chem.iitb.ac.in

Apparao Draksharapu – *Southern Laboratories, Department of Chemistry, Indian Institute of Technology Kanpur, Kanpur*

208016, India; orcid.org/0000-0001-7897-3230;
Email: appud@iitk.ac.in

Authors

Raju Eerlapally − *Southern Laboratories, Department of Chemistry, Indian Institute of Technology Kanpur, Kanpur 208016, India*

Purva Dua − *Department of Chemistry, Indian Institute of Technology Bombay, Mumbai 400076, India*

Divya Lakshmi Hareendran − *Southern Laboratories, Department of Chemistry, Indian Institute of Technology Kanpur, Kanpur 208016, India*

Asterios Charisiadis − *Instituto de Ciencia de Materiales de Madrid, Consejo Superior de Investigaciones Cienti′ficas, 28049 Madrid, Spain*

Lucia Velasco − *Instituto de Ciencia de Materiales de Madrid, Consejo Superior de Investigaciones Cienti′ficas, 28049 Madrid, Spain; Departamento de Química Física, Universidad Complutense de Madrid, 28040 Madrid, Spain*

Maxime Sauvan − *Instituto de Ciencia de Materiales de Madrid, Consejo Superior de Investigaciones Cienti′ficas, 28049 Madrid, Spain*

Indresh Verma − *Southern Laboratories, Department of Chemistry, Indian Institute of Technology Kanpur, Kanpur 208016, India*

Complete contact information is available at:
https://pubs.acs.org/10.1021/acs.inorgchem.5c01273

Author Contributions

The manuscript was written through the contributions of all authors. All authors have given approval to the final version of the manuscript.

Notes

The authors declare no competing financial interest.

■ ACKNOWLEDGMENTS

The research reported in this work is financially supported by SERB (CRG/2023/001112), and CSIR (01(3050)/21/EMR-II) to A.D. We thank the Department of Chemistry, IIT Kanpur, for the analytical facilities. R.E. and D.L.H. are grateful to IIT Kanpur for their institute fellowships. A.D. is grateful to Prof. Sayam Sen Gupta for helping us to record EPR. G.R. and P.D. thank IIT Bombay for the computational facility. D.M. acknowledges funding from the Ramon y Cajal grant RYC2020-029863-I through the Instituto de Ciencia de Materiales de Madrid, Consejo Superior de Investigaciones Cientificas (CSIC-ICMM), PIE grant from CSIC-ICMM (20226AT001), and the Spanish Ministerio de Ciencia, Innovación y Universidades grants (PID2019-111086RA-I00, TED2021-1327 57B-I00, PID2022-143013OB-I00, CNS2023-145046). L.V. acknowledges the Communidad de Madrid grant (PIPF-2022/ECO-25801) for a predoctoral fellowship.

■ REFERENCES

(1) Gribble, G. W. Biological Activity of Recently Discovered Halogenated Marine Natural Products. *Mar. Drugs* **2015**, *13* (7), 4044−4136.

(2) Paul, C.; Pohnert, G. Production and Role of Volatile Halogenated Compounds from Marine Algae. *Nat. Prod. Rep.* **2011**, *28* (2), 186−195.

(3) Rateb, M. E.; Ebel, R. Secondary Metabolites of Fungi from Marine Habitats. *Nat. Prod. Rep.* **2011**, *28* (2), 290−344.

(4) Blasiak, L. C.; Vaillancourt, F. H.; Walsh, C. T.; Drennan, C. L. Crystal Structure of the Non-Haem Iron Halogenase SyrB2 in Syringomycin Biosynthesis. *Nature* **2006**, *440* (7082), 368−371.

(5) Pandian, S.; Vincent, M. A.; Hillier, I. H.; Burton, N. A. Why Does the Enzyme SyrB2 Chlorinate, but Does Not Hydroxylate, Saturated Hydrocarbons? A Density Functional Theory (DFT) Study. *Dalton Trans.* **2009**, No. 31, 6201−6207.

(6) Vaillancourt, F. H.; Yin, J.; Walsh, C. T. SyrB2 in Syringomycin E Biosynthesis Is a Nonheme FeII α-Ketoglutarate- and O_2-Dependent Halogenase. *Proc. Natl. Acad. Sci. U. S. A.* **2005**, *102* (29), 10111−10116.

(7) Galonić, D. P.; Barr, E. W.; Walsh, C. T.; Bollinger, J. M.; Krebs, C. Two Interconverting Fe(IV) Intermediates in Aliphatic Chlorination by the Halogenase CytC3. *Nat. Chem. Biol.* **2007**, *3* (2), 113−116.

(8) Van Pée, K. H. Biosynthesis of Halogenated. *Biotechnology* **1996**, *50*, 375−399.

(9) Anderson, J. L. R.; Chapman, S. K. Molecular Mechanisms of Enzyme-Catalysed Halogenation. *Mol. Biosyst.* **2006**, *2* (8), 350−357.

(10) Cong, Z.; Yanagisawa, S.; Kurahashi, T.; Ogura, T.; Nakashima, S.; Fujii, H. Synthesis, Characterization, and Reactivity of Hypochloritoiron(III) Porphyrin Complexes. *J. Am. Chem. Soc.* **2012**, *134* (51), 20617−20620.

(11) Araki, I.; Fukui, K.; Fujii, H. Preparation, Characterization and Reactivity of a Bis-Hypochlorite Adduct of a Chiral Manganese(IV) Salen Complex. *Inorg. Chem.* **2018**, *57* (4), 1685−1688.

(12) Draksharapu, A.; Angelone, D.; Quesne, M. G.; Padamati, S. K.; Gõmez, L.; Hage, R.; Costas, M.; Browne, W. R.; De Visser, S. P. Identification and Spectroscopic Characterization of Nonheme Iron(III) Hypochlorite Intermediates. *Angew. Chem.- Int. Ed.* **2015**, *54* (14), 4357−4361.

(13) Draksharapu, A.; Codolà, Z.; Gómez, L.; Lloret-Fillol, J.; Browne, W. R.; Costas, M. Spectroscopic Analyses on Reaction Intermediates Formed during Chlorination of Alkanes with NaOCl Catalyzed by a Nickel Complex. *Inorg. Chem.* **2015**, *54* (22), 10656−10666.

(14) Corona, T.; Draksharapu, A.; Padamati, S. K.; Gamba, I.; Martin-Diaconescu, V.; Acuna-Parés, F.; Browne, W. R.; Company, A. Rapid Hydrogen and Oxygen Atom Transfer by a High-Valent Nickel-Oxygen Species. *J. Am. Chem. Soc.* **2016**, *138* (39), 12987−12996.

(15) Kumar, R.; Awasthi, A.; Gupta, S.; Eerlapally, R.; Draksharapu, A. Spectroscopic Characterization of a Ru(III)-OCl Intermediate: A Structural Mimic of Haloperoxidase Enzymes. *Dalton Trans.* **2022**, *51* (34), 12848−12854.

(16) Kumar, R.; Ahsan, F.; Awasthi, A.; Swart, M.; Draksharapu, A. Generation of Ru(III)-Hypochlorite with Resemblance to the Heme-Dependent Haloperoxidase Enzyme. *Dalton Trans.* **2023**, *52* (35), 12552−12559.

(17) Chiang, C. Y.; Ohashi, M.; Le, J.; Chen, P. P.; Zhou, Q.; Qu, S.; Bat-Erdene, U.; Hematian, S.; Rodriguez, J. A.; Houk, K. N.; Guo, Y.; Loo, J. A.; Tang, Y. Copper-Dependent Halogenase Catalyses Unactivated C−H Bond Functionalization. *Nature* **2025**, *638*, 126−132.

(18) (a) Eerlapally, R.; Gupta, S.; Awasthi, A.; Kumar, R.; Draksharapu, A. Spectroscopic Characterization and the Reactivity of a High Valent (L)Cu(III) Species Supported by a Proline-Based Pseudopeptide. *Dalton Trans.* **2023**, *52* (25), 8645−8653. (b) Shakya, R.; Jozwiuk, A.; Powell, D. R.; Houser, R. P. Synthesis and Characterization of Polynuclear Copper(II) Complexes with Pyridylbis(Phenol) Ligands. *Inorg. Chem.* **2009**, *48* (9), 4083−4088. (c) Singh, J.; Hundal, G.; Gupta, R. Studies on Nickel(II) Complexes with Amide-Based Ligands: Syntheses, Structures, Electrochemistry and Oxidation Chemistry. *Eur. J. Inorg. Chem.* **2008**, *2008*, 2052−2063. (d) Sharma, S. K.; Upreti, S.; Gupta, R. Effect of Ligand Architecture on the Structure and Properties of Square-Planar Nickel(II) Complexes of Amide-Based Macrocycles. *Eur. J. Inorg. Chem.* **2007**, *2007*, 3247−3259. (e) Burguete, M. I.; Galindo, F.; Luis,

S. V.; Vigara, L. A Turn-on Fluorescent Indicator for Citrate with Micromolar Sensitivity. *Dalton Trans.* **2007**, *36*, 4027−4033.

(19) Gorla, L.; Martí-Centelles, V.; Freimuth, L.; Altava, B.; Burguete, M. I.; Luis, S. V. Cu^{2+}, Zn^{2+}, and Ni^{2+} Complexes of C_2-Symmetric Pseudopeptides with an Aromatic Central Spacer. *Inorg. Chem.* **2016**, *55* (15), 7617−7629.

(20) Nayak, Y. N.; Gaonkar, S. L.; Saleh, E. A. M.; Dawsari, A. M. A. L.; Harshitha; Husain, K.; Hassan, I. Chloramine-T (N-Chloro-p-Toluenesulfonamide Sodium Salt), a Versatile Reagent in Organic Synthesis and Analytical Chemistry: An up to Date Review. *J. Saudi Chem. Soc.* **2022**, *26* (2), No. 101416.

(21) Anson, F. C.; Collins, T. J.; Richmond, T. G.; Santarsiero, B. D.; Toth, J. E.; T Treco, B. G. R. Highly Stabilized Copper(III) Complexes. *J. Am. Chem. Soc.* **1987**, *109* (10), 2974−2979.

(22) Garrido-Barros, P.; Moonshiram, D.; Gil-Sepulcre, M.; Pelosin, P.; Gimbert-Suriñach, C.; Benet-Buchholz, J.; Llobet, A. Redox Metal-Ligand Cooperativity Enables Robust and Efficient Water Oxidation Catalysis at Neutral pH with Macrocyclic Copper Complexes. *J. Am. Chem. Soc.* **2020**, *142* (41), 17434−17446.

(23) Birkelbach, F.; Winter, M.; Florke, U.; Haupt, H. J.; Butzlaff, C.; Lengen, M.; Bill, E.; Trautwein, A. X.; Wieghardt, K.; Chaudhuri, P. Exchange Coupling in Homo- and Heterodinuclear Complexes CunM [M = Cr(III), Mn(III),Mn(II), Fe(III), Co(III), Co(II), Ni(II), Cu(II), Zn(II)]. Synthesis, Structures, and Spectroscopic Properties. *Inorg. Chem.* **1994**, *33* (18), 3990−4001.

(24) (a) Solomon, E. I.; Szilagyi, R. K.; DeBeer George, S.; Basumallick, L. Electronic Structures of Metal Sites in Proteins and Models: Contributions to Function in Blue Copper Proteins. *Chem. Rev.* **2004**, *104* (2), 419−458. (b) DeBeer George, S.; Basumallick, L.; Szilagyi, R. K.; Randall, D. W.; Hill, M. G.; Nersissian, A. M.; Valentine, J. S.; Hedman, B.; Hodgson, K. O.; Solomon, E. I. Spectroscopic Investigation of Stellacyanin Mutants: Axial Ligand Interactions at the Blue Copper Site. *J. Am. Chem. Soc.* **2003**, *125* (37), 11314−11328. (c) Kau, L. S.; Spira-solomon, D. J.; Spira-solomon-penner-hahn, J. E.; Hodgson, K. O.; Solomon, E. I. X-Ray Absorption Edge Determination of the Oxidation State and Coordination Number of Copper: Application to the Type 3 Site in Rhus Vernicifera Laccase and Its Reaction with Oxygen. *J. Am. Chem. Soc.* **1987**, *109* (21), 6433−6442.

(25) (a) Dubois, J. L.; Mukherjee, P.; Collier, A. M.; Mayer, J. M.; Solomon, E. I.; Hedman, B.; Stack, T. D. P.; Hodgson, K. O.; V, S. U.; V, S. U.; May, R. V. Cu K-Edge XAS Study of the $[Cu_2(\mu\text{-}O)_2]$ Core: Direct Experimental Evidence for the Presence of Cu(III). *J. Am. Chem. Soc.* **1997**, *119* (36), 8578−8579. (b) Garrido-Barros, P.; Gimbert-Surinifach, C.; Moonshiram, D.; Picón, A.; Monge, P.; Batista, V. S.; Llobet, A. Electronic π-Delocalization Boosts Catalytic Water Oxidation by Cu(II) Molecular Catalysts Heterogenized on Graphene Sheets. *J. Am. Chem. Soc.* **2017**, *139* (37), 12907−12910. (c) Garrido-Barros, P.; Moonshiram, D.; Gil-Sepulcre, M.; Pelosin, P.; Gimbert-Suriñach, C.; Benet-Buchholz, J.; Llobet, A. Redox Metal-Ligand Cooperativity Enables Robust and Efficient Water Oxidation Catalysis at Neutral pH with Macrocyclic Copper Complexes. *J. Am. Chem. Soc.* **2020**, *142* (41), 17434−17446.

(26) DuBois, J. L.; Mukherjee, P.; Stack, T. D. P.; Hedman, B.; Solomon, E. I.; Hodgson, K. O. A Systematic K-Edge X-Ray Absorption Spectroscopic Study of Cu(III) Sites. *J. Am. Chem. Soc.* **2000**, *122* (24), 5775−5787.

(27) Lim, H.; Thomas, K. E.; Hedman, B.; Hodgson, K. O.; Ghosh, A.; Solomon, E. I. X-Ray Absorption Spectroscopy as a Probe of Ligand Noninnocence in Metallocorroles: The Case of Copper Corroles. *Inorg. Chem.* **2019**, *58* (10), 6722−6730.

(28) Kaur, S.; Das, A.; Velasco, L.; Sauvan, M.; Bera, M.; Ugale, A.; Charisiadis, A.; Moonshiram, D.; Paria, S. Spectroscopic Characterization and Reactivity Studies of a Copper(II) Iminoxyl Radical Complex. *Chem. Commun.* **2024**, *60* (73), 9934−9937.

(29) Comba, P.; Faltermeier, D.; Martin, B. Computational Approaches for Redox Potentials of Iron(IV)-Oxido Complexes. *Z. Anorg. Allg. Chem.* **2020**, *646* (22), 1839−1845.

(30) Bogojeski, M.; Vogt-Maranto, L.; Tuckerman, M. E.; Müller, K. R.; Burke, K. Quantum Chemical Accuracy from Density Functional Approximations via Machine Learning. *Nat. Commun.* **2020**, *11* (1), No. 5223.

(31) Wu, T.; Macmillan, S. N.; Rajabimoghadam, K.; Siegler, M. A.; Lancaster, K. M.; Garcia-Bosch, I. Structure, Spectroscopy, and Reactivity of a Mononuclear Copper Hydroxide Complex in Three Molecular Oxidation States. *J. Am. Chem. Soc.* **2020**, *142* (28), 12265−12276.

(32) Mondal, P.; Lovisari, M.; Twamley, B.; McDonald, A. R. Fast Hydrocarbon Oxidation by a High-Valent Nickel−Fluoride Complex. *Angew. Chem.- Int. Ed.* **2020**, *59* (31), 13044−13050.

(33) McManus, C.; Mondal, P.; Lovisari, M.; Twamley, B.; McDonald, A. R. Carboxamidate Ligand Noninnocence in Proton Coupled Electron Transfer. *Inorg. Chem.* **2019**, *58* (7), 4515−4523.

(34) Darcy, J. W.; Koronkiewicz, B.; Parada, G. A.; Mayer, J. M. A Continuum of Proton-Coupled Electron Transfer Reactivity. *Acc. Chem. Res.* **2018**, *51* (10), 2391−2399.

(35) Barman, P.; Vardhaman, A. K.; Martin, B.; Wörner, S. J.; Sastri, C. V.; Comba, P. Influence of Ligand Architecture on Oxidation Reactions by High-Valent Nonheme Manganese Oxo Complexes Using Water as a Source of Oxygen. *Angew. Chem., Int. Ed.* **2015**, *54*, 2095−2099.

(36) Dolomanov, O. V.; Bourhis, L. J.; Gildea, R. J.; Howard, J. A. K.; Puschmann, H. OLEX2: a complete structure solution, refinement and analysis program. *J. Appl. Crystallogr.* **2009**, *42*, 339−341.

(37) Sheldrick, G. M. SHELXT − Integrated space-group and crystal structure determination. *Acta Crystallogr., Sect. A: Found. Adv.* **2015**, *71*, 3−8.

(38) Ravel, B.; Newville, M. ATHENA, ARTEMIS, HEPHAESTUS: data analysis for X-ray absorption spectroscopy using IFEFFIT. *J. Synchrotron. Radiat.* **2005**, *12*, 537−541.

(39) Rehr, J. J.; Albers, R. C. Theoretical Approaches to X-Ray Absorption Fine Structure. *Rev. Mod. Phys.* **2000**, *72* (3), 621−654.

(40) Frisch, M. J.; Trucks, G. W.; Schlegel, H. B.; Scuseria, G. E.; Robb, M. A.; Cheeseman, J. R.; Scalmani, G.; Barone, V.; Petersson, G. A.; Nakatsuji, H.; Li, X.; Caricato, M.; Marenich, A. V.; Bloino, J.; Janesko, B. G.; Gomperts, R.; Mennucci, B.; Hratchian, H. P.; Ortiz, J. V.; Izmaylov, A. F.; Sonnenberg, J. L.; Williams-Young, D.; Ding, F.; Lipparini, F.; Egidi, F.; Goings, J.; Peng, B.; Petrone, A.; Henderson, T.; Ranasinghe, D.; Zakrzewski, V. G.; Gao, J.; Rega, N.; Zheng, G.; Liang, W.; Hada, M.; Ehara, M.; Toyota, K.; Fukuda, R.; Hasegawa, J.; Ishida, M.; Nakajima, T.; Honda, Y.; Kitao, O.; Nakai, H.; Vreven, T.; Throssell, K.; Montgomery, J. A., Jr.; Peralta, J. E.; Ogliaro, F.; Bearpark, M. J.; Heyd, J. J.; Brothers, E. N.; Kudin, K. N.; Staroverov, V. N.; Keith, T. A.; Kobayashi, R.; Normand, J.; Raghavachari, K.; Rendell, A. P.; Burant, J. C.; Iyengar, S. S.; Tomasi, J.; Cossi, M.; Millam, J. M.; Klene, M.; Adamo, C.; Cammi, R.; Ochterski, J. W.; Martin, R. L.; Morokuma, K.; Farkas, O.; Foresman, J. B.; Fox, D. J. *Gaussian 16, Revision C.01*.

(41) Becke, A. D. Density-Functional Thermochemistry. V. Systematic Optimization of Exchange-Correlation Functionals. *J. Chem. Phys.* **1997**, *107*, 8554−8560.

(42) Antony, J.; Grimme, S. Density Functional Theory Including Dispersion Corrections for Intermolecular Interactions in a Large Benchmark Set of Biologically Relevant Molecules. *Phys. Chem. Chem. Phys.* **2006**, *8* (45), 5287−5293.

(43) Tomasi, J.; Mennucci, B.; Cammi, R. Quantum Mechanical Continuum Solvation Models. *Chem. Rev.* **2005**, *105* (8), 2999−3093.

(44) Zhurko, G.; Zhurko, D. *ChemCraft, Version 1.8, Build 682*, http://www.chemcraftprog.com.

(45) Gorla, L.; Martí-Centelles, V.; Freimuth, L.; Altava, B.; Burguete, M. I.; Luis, S. V. Cu^{2+}, Zn^{2+}, and Ni^{2+} Complexes of C_2-Symmetric Pseudopeptides with an Aromatic Central Spacer. *Inorg. Chem.* **2016**, *55* (15), 7617−7629.